Monolayer Amphiphiles Hydrophobicize MoS 2 -Mediated Real-Time Water Removal for Efficient Waterproof Hydrogen Detection

Zongke Li, Xiao Wu, Wen Wang, Xiaoming Wen, Feng Niu, Dandan Han, Wei Zhong, Vitaly Ordomsky, Qiyan Wang, Ronghan Wei, et al.

Monolayer Amphiphiles Hydrophobicize MoS 2 - Mediated Real-Time Water Removal for Efficient Waterproof Hydrogen Detection

Zongke Li[a,1], Xiao Wu[a,1], Wen Wang[a], Xiaoming Wen[b], Feng Niu[c], Dandan Han[d], Wei Zhong[a], Vitaly V. Ordomsky[e], Qiyan Wang[a], Ronghan Wei[a], Tianshui Liang[a].*

[a]*College of Mechanics and Safety Engineering, Zhengzhou University, Henan 450001, China;*

[b]*College of Mechanics and Safety Engineering, Zhengzhou University, Henan 450001, China;*

[c]*College of Materials and Chemistry, China Jiliang University, Zhejiang 310018, China;*

[d] *College of Science, Henan Agricultural University, 450002, China;*

[e] *Univ. Lille, CNRS, Centrale Lille, ENSCL, Univ. Artois, UMR 8181-UCCS-Unit´e de Catalyse et Chimie du Solide, F-59000 Lille, France.*

[1]*equal contribution; *correspondence author.*

Abstract

Ensuring the water fouling-free operation of semiconductor-based gas sensors is crucial to maintaining their accuracy, reliability, and stability across various applications. However, achieving a balance between waterproofing and timely leak detection remains challenging in terms of current hydrophobic strategies. Herein, we construct a novel waterproof H_2 sensor by integrating single-atom $Ru^{(III)}$ self-assembly with hydrophobic monolayer micelles embedded in MoS_2. The unique monolayer structure enables the sensor to detect H_2 in the presence of water, as well as facilitating the self-transport of in-situ generated water from the H_2-O_2 reaction during H_2 detection. Simultaneously, single-atom $Ru^{(III)}$ exhibits high H_2 dissociation ability and works synergistically with monolayer micelles of efficient H_2 enrichment, reducing the response time to 3.5 s, compared to 21 s for pristine MoS_2 and 9.7 s for multilayer micelles. Deployable on mobile platforms, it enables wireless H_2 detection for up to 6 months, without introduction of protective membranes against dust and water ingress. This work significantly broadens the utility of semiconductor-based gas sensors for rapid gas detection in harsh environments.

KEYWORDS: Waterproof H_2 detection, $Ru^{(III)}$ single atoms, monolayer micelle, in-situ water transport, room temperature.

Introduction

Hydrogen (H_2), a clean and renewable energy carrier, is increasingly utilized for vehicle propulsion and electrical energy storage[1]. However, its high flammability requires efficient monitoring sensors[2]. Semiconductor-based sensors are widely used for this purpose due to their fast response, durability and affordability compared to other types [3]. However, in outdoor or harsh environment, such as industrial sites, farmland, and mine fields, semiconductor-based sensors are vulnerable to wet conditions like rain, high humidity, or liquid splashes [4], which largely shortens their service life. Hydrophobicizing the semiconductor-based sensors not only solves the problem of external water intrusion and extends the service life of the sensor, but also improves the H_2 concentration of sensing sites and resistance to interference from other gases[5].

One common method to achieve hydrophobicity involves modifying metal oxide/sulfide semiconductors with organic functional groups[4a, 6]. Monomers like organosilanes[7], reduced graphene oxide(rGO) [8], poly(vinylidene fluoride)[9], and trimethylaluminum [10] are used to modify or deposit onto semiconductor surfaces to make them hydrophobic and repel water molecules. This prevents water adsorption, thereby reducing the risk of degradation in wet environments, ensuring long-term reliability and durability of the semiconductor-based gas sensor. However, controlling the thickness of the modification layer during surface modification is a challenge. Excessively thick hydrophobic layer reduces rapid diffusion of gases to the sensing sites, increasing sensor response time-a critical parameter, especially in applications that require fast detection [11]. Besides, during H_2 detection, water produced from the

H_2-O_2 interaction tends to localize under a thick hydrophobic layer, decreasing sensitivity and stability[12]. These issues highlight the need for further investigation and consideration in sensor design and optimization strategies.

In this study, we construct a novel waterproof semiconductor-based H_2 sensor by self-assembly a hydrophobic monolayer of micelles on the MoS_2 surface. The single-atom $Ru^{(III)}$ acts as an active site, displaying high H_2 dissociation ability during H_2 detection, while the monolayer micelles enable H_2 enrichment over the $Ru^{(III)}$ active site and facilitate directional transport of external/internal water. Conversely, multilayer micelles grafted on MoS_2 makes the sensor hydrophilic, significantly decreasing its detection performance. When deployed on mobile platforms like cars and drones, this sensor achieves wireless H_2 detection even after six months of exposure, eliminating the need for protective membranes against dust and water ingress. This study not only enhances the performance of H_2 detection, but also introduces new idea for the advancement of stable water-sensitive sensors.

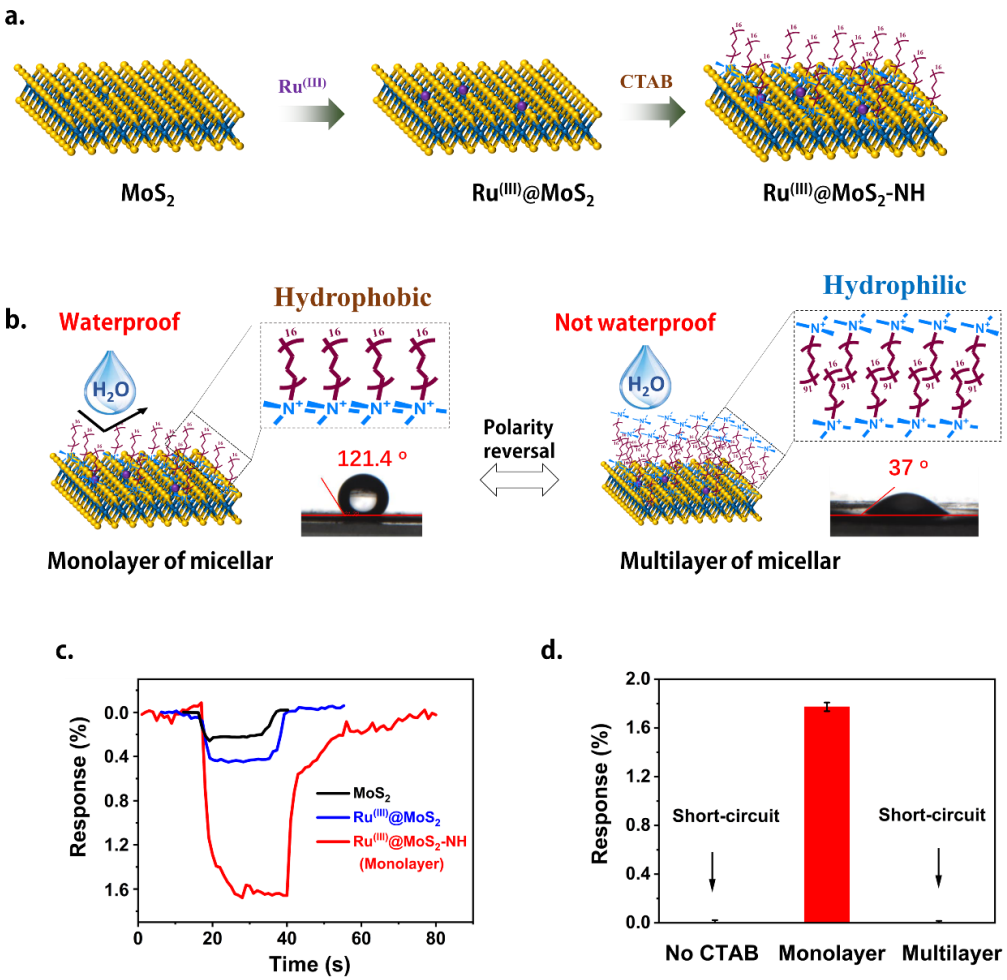

Figure 1. *Schematic depicting Ru$^{(III)}$@MoS$_2$-NH with hydrophobic monolayer for waterproof H_2 detection. a) Self-assembled process of Ru$^{(III)}$@MoS$_2$-NH with hydrophobic monolayer micelle. b) Hydrophobicity of Ru$^{(III)}$@MoS$_2$-NH monolayer and multilayer micelles on the MoS$_2$ surface. c) Compared with other MoS$_2$-based materials, Ru$^{(III)}$@MoS$_2$-NH with monolayer micelles exhibits higher performance in H_2 response. d) Thickness of the micelle layer affects the H_2 response of Ru$^{(III)}$@MoS$_2$-NH in presence of water. H_2 response condition: 30 °C, 0.5% Ru, and 1000 ppm H_2.*

Results and discussion

3.1 Structural basis of Ru$^{(III)}$@MoS$_2$-NH with H_2 response.

According to our previous work, Ru-based functional materials modified with micelles had demonstrated excellent hydrophobic performance in chemical reactions[13].

These findings inspired us to apply this strategy to H_2 sensing reactions to prevent water intrusion of sensing sites. As a result, we developed a novel waterproof H_2 sensing material synthesized by self-assembling hydrophobic monolayer micelles with $Ru^{(III)}$ over MoS_2, devoted as $Ru^{(III)}$@MoS_2-NH(Monolayer) (**Figure 1**). Within this material, single-atom $Ru^{(III)}$ served as an sensing active site, exhibiting high H_2 dissociation ability during detection. MoS_2 accepted electrons generated by H_2 decomposition to convert sensing signals, while the monolayer micelle structure facilitated the directional transport of external/internal water to prevent its intrusion into the sensing site.

First, the size and morphology of Ru in $Ru^{(III)}$@MoS_2-NH(Monolayer) were characterized using STEM-HAADF (**Figure 2**). STEM-HAADF images revealed a well-defined hexagonal structure corresponding to the 2H structure of MoS_2, consistent with XRD (**Figure S1a, SI**) and TEM observations (**Figure S2a-f, SI**). Because of the high sensitivity to the Z atomic number[14], STEM-HAADF was particularly suited to assess the Ru distribution. Magnified images clearly showed bright spots on the surface of MoS_2, indicative of single Ru atoms (**Figure 2a**, **Figure 2c** and **Figure S2g-h, SI**). The presence of atomic Ru dispersion had been additionally confirmed by EDS mappings (**Figure 2d**).

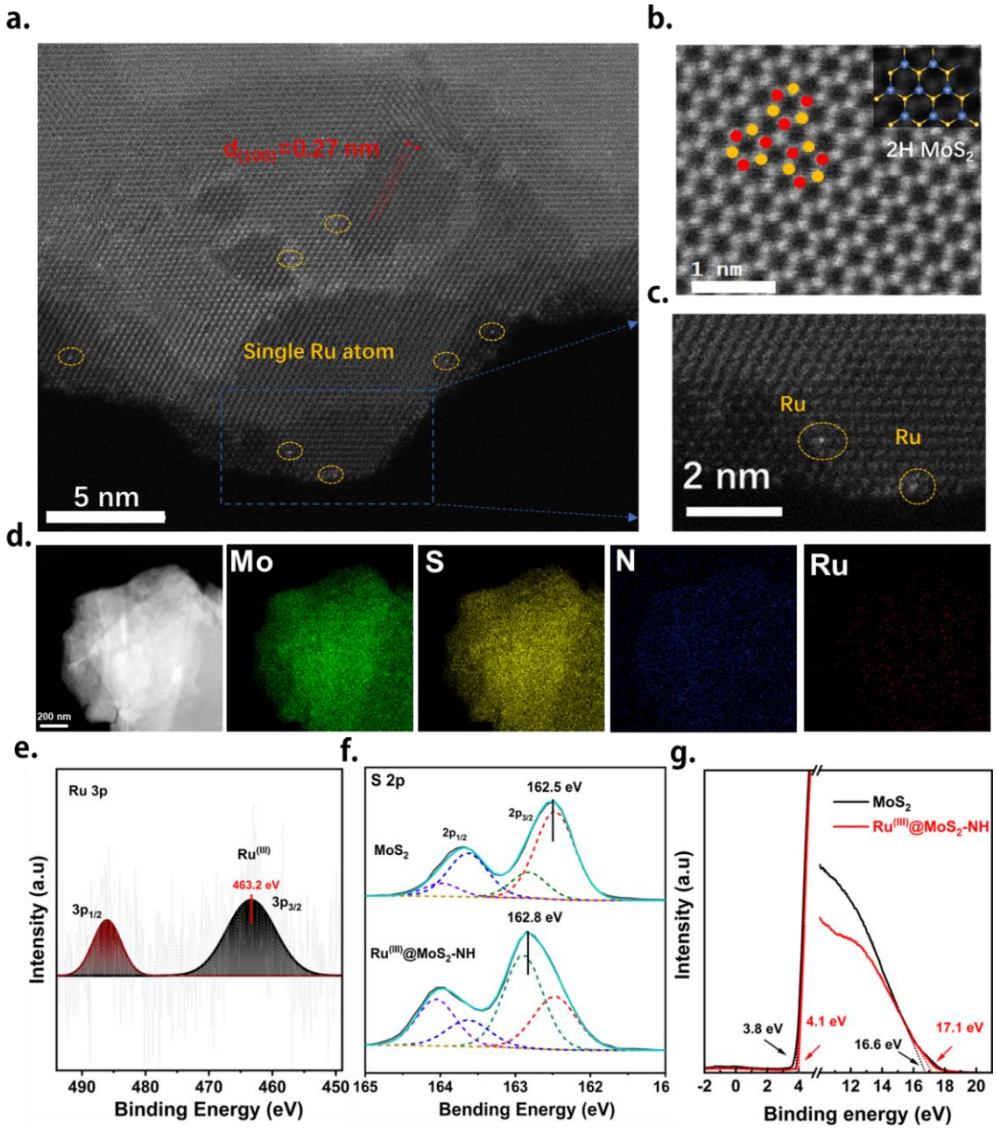

Figure 2. *Characterization structure of $Ru^{(III)}@MoS_2$-NH with $Ru^{(III)}$ single atoms. a-b) HAADF-STEM image of $Ru^{(III)}@MoS_2$-NH, and c) its corresponding enlarged image. d) EDS mappings of $Ru^{(III)}@MoS_2$-NH for Mo, S, N and Ru. e) XPS Ru 3p and f) S 2p of the MoS_2 and $Ru^{(III)}@MoS_2$-NH. g) Band alignment of MoS_2 and $Ru^{(III)}@MoS_2$-NH determined from UPS data. Characterized material $Ru^{(III)}@MoS_2$-NH contains 0.5% Ru and monolayer micelle.*

The electronic state of Ru in $Ru^{(III)}@MoS_2$-NH(Monolayer) had been further studied by XPS (**Figure 2e**). Analysis of the Ru $3p_{3/2}$ spectra revealed a characteristic peak at 463.2 eV, indicative of Ru existing in the oxidation state of Ru^{3+} [15]. Notably, an electron transfer phenomenon between Ru and MoS_2 was identified, as evidenced

by the apparent change in S $2p_{3/2}$ from 162.5 eV for pristine MoS_2 to 162.8 eV for $Ru^{(III)}$@MoS_2-NH(Monolayer)[16] (**Figure 2f**). This phenomenon was further proved by the UPS (**Figure 2g** and **Figure S1d, SI**). In the valence band region (left), a discernible shift from 3.8 eV to 4.1 eV was observed for MoS_2 and $Ru^{(III)}$@MoS_2-NH(Monolayer)[17], respectively.

Then, to elucidate the distribution of micelles within $Ru^{(III)}$@MoS_2-NH(Monolayer), the structure of the MoS_2 layer was analyzed. Raman spectra and TG analysis (**Figure S1b-c, SI**) verified the presence of cetyltrimethylammonium bromide (CTAB) micelles in $Ru^{(III)}$@MoS_2-NH(Monolayer), evidenced by characteristic C-H vibration peaks at 2780 cm^{-1} [13a] and a 10% weight loss. Raman spectra was further conducted for analysis of MoS_2 layer, and the results indicated an expanded layer spacing compared to pristine MoS_2. The gap between the E^1_{2g} (378 cm^{-1}) and A_{1g} (410 cm^{-1}) modes of 25.5 cm^{-1}, slightly smaller than observed for MoS_2 (**Figure S3a, SI**)[18]. STEM-HAADF analysis demonstrated a gradual increase in interlayer spacing, ranging from 0.62 nm to 0.74 nm for thicker configurations (**Figure S4, SI**). SAXS analysis (**Figure S3b-d, SI**) confirmed this, showing increased intensity at 0.05-0.2 nm for $Ru^{(III)}$@MoS_2-NH(Monolayer), possibly due to the presence of micelles inserting into the MoS_2 layer[19].

To gain deeper insights into the micelle structure within $Ru^{(III)}$@MoS_2-NH(Monolayer), we conducted a model experiment using micelle-modified MoS_2 deposited on a wafer to investigate micelle thickness (**Figure 3**). AFM evaluation revealed that compared to pristine MoS_2, the surface roughness of Micelle@MoS_2 was

higher, with a difference of 2.6 nm, corresponding to the height of a monolayer CTAB molecule at 2.5 nm (**Figure 3a-b** and **Figure S5, SI**) [20]. Remarkably, increasing the surfactant concentration resulted in the formation of bilayer micelles over the MoS_2 surface. AFM studies indicated a micelle height of 4.6 nm, shorter than the height of a bilayer molecule at 5 nm due to crossovers between molecular layers (**Figure 3a**, **Figure 3c** and **Figure S5, SI**). These findings were consistent with STEM-HAADF and AFM results, further confirming the monolayer micelle structure of $Ru^{(III)}$@MoS_2-NH(Monolayer).

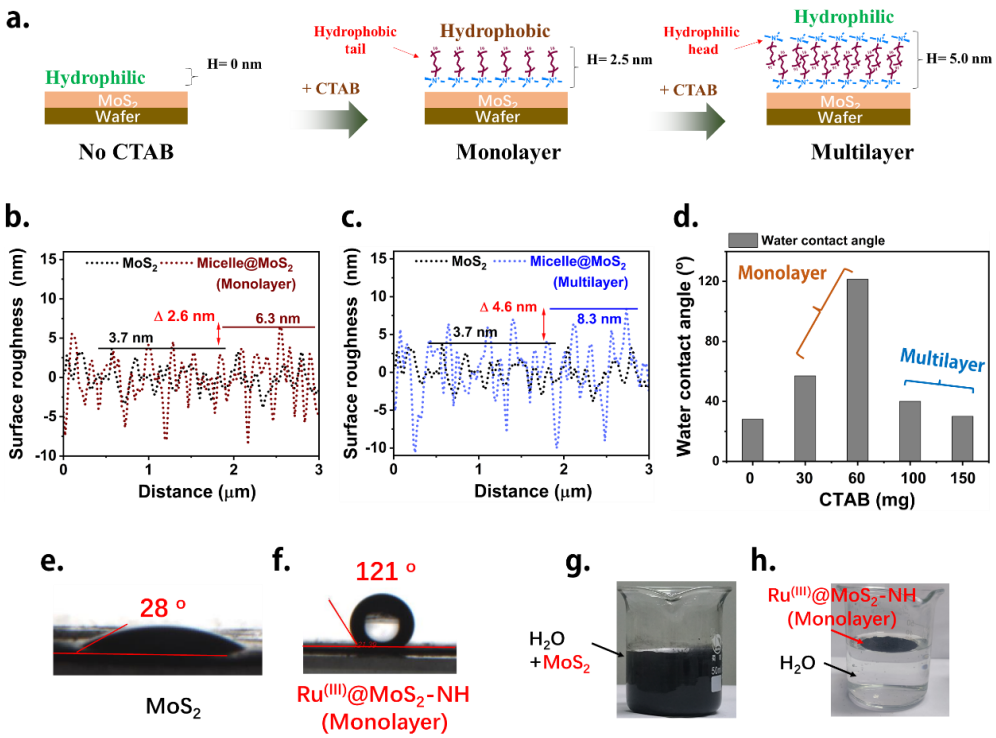

Figure 3. *Characterization hydrophobic layer structure of $Ru^{(III)}$@MoS_2-NH. a) Deposition process of micelle-modified MoS_2 on a wafer and the thickness of the micelle layer as depicted by AFM (b) monolayer and c) multilayer. d) Hydrophobic of $Ru^{(III)}$@MoS_2-NH as a function of micelle thickness. photographs of water contact angle for e) MoS_2 and f) $Ru^{(III)}$@MoS_2-NH. Photographs of g) MoS_2 and h) $Ru^{(III)}$@MoS_2-NH dispersed in water. Characterized material $Ru^{(III)}$@MoS_2-NH*

contains 0.5% Ru.

After that, surface hydrophobicity assessments were conducted via water-droplet contact angle tests for $Ru^{(III)}$@MoS_2-NH(Monolayer) and MoS_2 (**Figure 3d-f**). MoS_2 exhibited a contact angle of 28°, indicating its hydrophilic nature. Upon self-assembly of micelles, the contact angle of $Ru^{(III)}$@MoS_2-NH (Monolayer) significantly increased to 121°, confirming its transformation into a hydrophobic material. Interestingly, the hydrophobicity of $Ru^{(III)}$@MoS_2-NH decreased as the CTAB amount increased, from 121° decreased to 30° (**Figure 3d** and **Figure S6b, SI**). This phenomenon also observed in model experiments of micelle-modified MoS_2 deposited on a wafer, the hydrophobicity of MoS_2 decreased as number of layers increased (**Figure S6a, SI**). The formation of bilayer micelles over MoS_2 resulted in increased hydrophilicity, likely due to the distribution of hydrophilic heads on the outer layer, similar to the structure of cell membranes (**Figure 3a**)[21]. Additionally, compared to MoS_2, $Ru^{(III)}$@MoS_2-NH(Monolayer) exhibited resistance to water penetration, maintaining a distinct phase for up to 2 weeks (**Figure 3g-h** and **Figure S7, SI**).

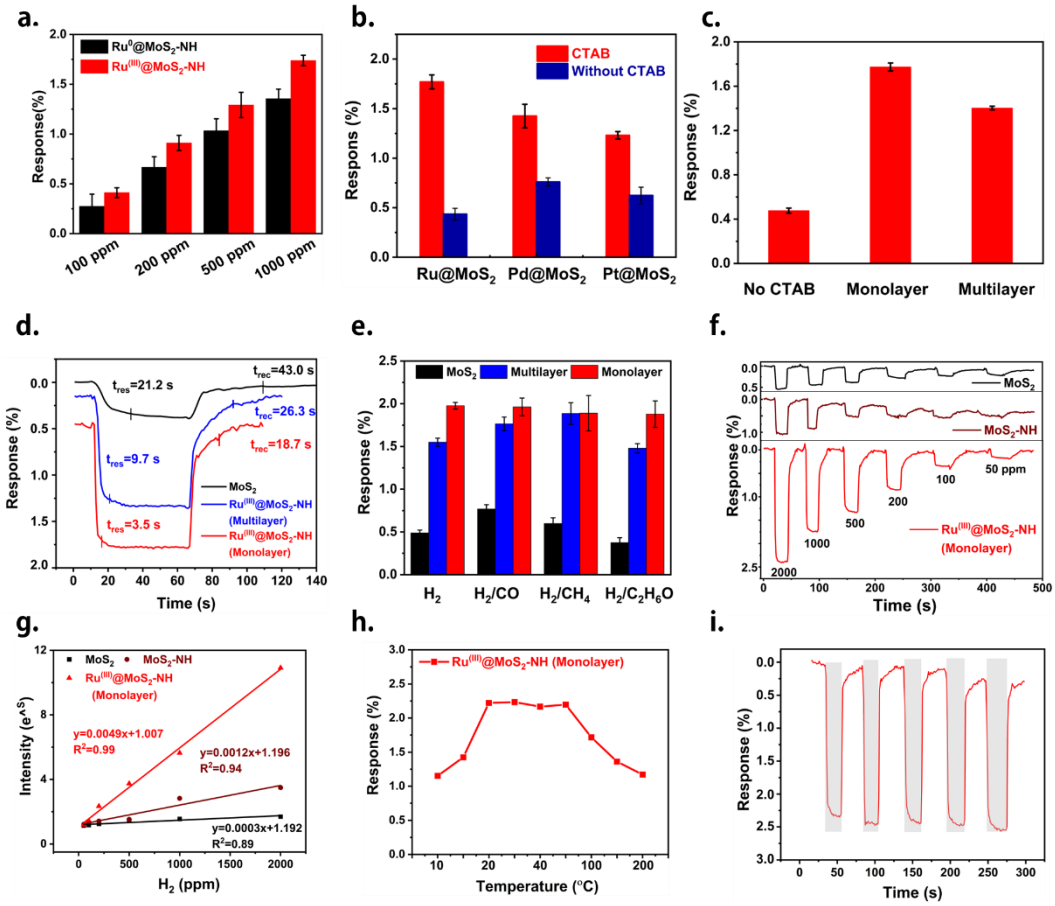

Figure 4. *H_2 detection performance of $Ru^{(III)}$@MoS_2-NH. Effects of a) Ru state, b) metal species, and c) micelle thickness on the H_2 response of $Ru^{(III)}$@MoS_2-NH. d) Amplified response curves and e) anti-interference curves of $Ru^{(III)}$@MoS_2-NH with different micelle thicknesses. f) Real-time H_2 response of MoS_2, MoS_2-NH and $Ru^{(III)}$@MoS_2-NH(Monolayer), and g) its linear fitting curves. h) Temperature and j) repeatability of $Ru^{(III)}$@MoS_2-NH(Monolayer) for H_2 response. H_2 response condition:1000 ppm H_2 for b-e), but 2000 ppm H_2 for h-i), temperature of a-g) & i) at 30 °C, metals content at 0.5% for all test.*

3.2 H_2 sensing performance of Ru $^{(III)}$@MoS_2-NH.

The factors influencing gas sensing performance of $Ru^{(III)}$@MoS_2-NH were investigated first. Comparative analysis of reduced Ru^0 and oxidized $Ru^{(III)}$ shows that $Ru^{(III)}$ exhibits enhanced H_2 response in the concentration range from 100 ppm to 1000 ppm, which be attributed to the easy dissociation of H_2 into H* and e^- over the $Ru^{(III)}$

active site (**Figure 4a**)[13a, 22]. Additionally, Ru demonstrated superior H_2 response at 1.7%, surpassing various metals such as Pd (1.2%) and Pt (1.0%)-a finding consistent with previous studies highlighting Ru's efficacy in H_2 dissociation at low temperatures (**Figure S8a, SI**) [13a]. Interestingly, the presence of CTAB micelles significantly enhanced the H_2 response on sensors composed of these metals@MoS_2-NH (**Figure 4b** and **Figure S8b, SI**), indicative of hydrophobic metals@MoS_2-NH facilitating increased H_2 absorption[23]. However, higher CTAB content in $Ru^{(III)}$@MoS_2-NH (Multilayer) reduced its H_2 response from 1.7% to 1.5%, attributed to the decreased H_2 enrichment caused by the hydrophilic outer layer (**Figure 1d** and **Figure 4c**). Furthermore, the influence of Ru content was investigated (**Figure S8b, SI**), revealing optimal performance at 0.5% Ru content, corresponding to atomic Ru dispersion. Higher Ru contents (ranging from 0.5% to 1%) resulted in agglomeration into larger Ru particles (**Figure S2h, SI**), reducing the exposed surface area available for H_2 interaction. Conversely, too lower Ru content exhibited reduced H_2 response attributed to fewer active H_2 dissociation sites[24].

Furthermore, the $Ru^{(III)}$@MoS_2-NH(Monolayer) sensor exhibited superior performance in H_2 sensing. It showed an impressive H_2 response time of 3.5 s and rapid recovery time of 18.7 s, significantly enhancing the sensor's response capability compared to MoS_2 and $Ru^{(III)}$@MoS_2-NH(Multilayer) (**Figure 4d** and **Figure S8c-d, SI**). Additionally, $Ru^{(III)}$@MoS_2-NH(Monolayer) displayed high H_2 response compared to other gases, accurately distinguishing H_2 even in the presence of equivalent concentrations of CO, CH_4, and ethanol, minimizing the possibility of H_2 false positives

(**Figure 4f** and **Figure S9, SI**). This enhanced performance is may attributed to the hydrophobic monolayer micelle structure of $Ru^{(III)}$@MoS_2-NH(Monolayer), which facilitates fast response and resistance to interference from other gases. $Ru^{(III)}$@MoS_2-NH(Monolayer) also exhibited a linear characteristics of H_2 response over wide concentration range from 50 ppm to 2000 ppm, with a R^2 value of 0.99 (**Figure 4g** and **Figure 4h**). Notably, the sensor maintained consistent H_2 response at 2.2% over a broad temperature (20-80 °C) at 2000 ppm H_2, effectively mitigating disturbances caused by temperature fluctuations (**Figure 4i**). Demonstrated repeatability in **Figure 4j** revealed consistent H_2 response around 2.4% over 5 cycles at 2000 ppm H_2, emphasizing the excellent reversibility and repeatability of the sensor.

The waterproof H_2 detection performance of $Ru^{(III)}$@MoS_2-NH(Monolayer) illustrated in **Figure 5**. While the hydrophilic MoS_2 exhibited weak H_2 response, the presence of water droplets induced a short circuit, leading to no H_2 response (**Figure 5a-b**). In contrast, the hydrophobic $Ru^{(III)}$@MoS_2-NH(Monolayer) maintained consistent H_2 response before and after water droplet added, even after 60 minutes in presence of water (**Figure 5c-d**). Furthermore, a water immersion experiment was conducted to verify the superhydrophobic H_2 detection capability of $Ru^{(III)}$@MoS_2-NH(Monolayer) (**Figure 5e-g**). Initially, the $Ru^{(III)}$@MoS_2-NH(Monolayer) displayed a resistance of 0.98 kΩ and high H_2 response (**Figure 5e**). Upon immersion in water, it maintained almost the same resistance of 0.99 kΩ without short circuiting (**Figure 5f**) and with same H_2 response compared to before immersion. Upon removal from the

aqueous medium, the $Ru^{(III)}$@MoS_2-NH(Monolayer) sensor maintained its resistance of 0.94 kΩ and retained the same H_2 response as prior to immersion (**Figure 5g**).

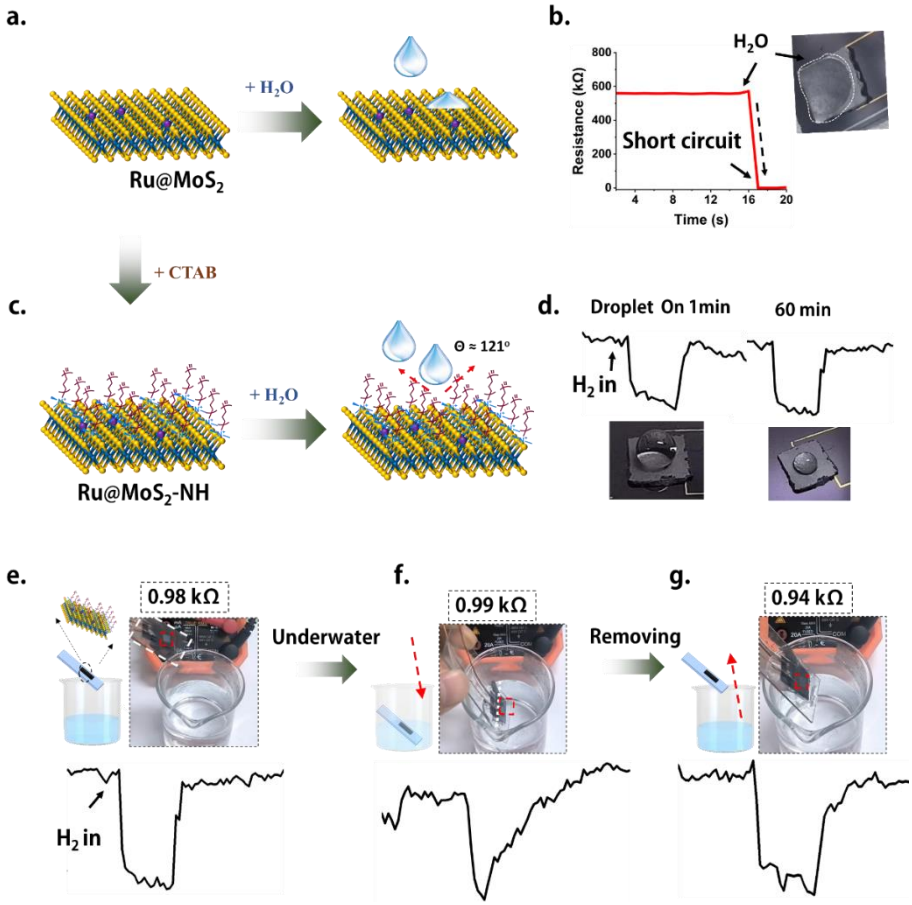

Figure 5. *Waterproof H_2 detection performance of the $Ru^{(III)}$@MoS_2-NH(Monolayer). H_2 response of a-b) MoS_2 and c-d) $Ru^{(III)}$@MoS_2-NH(Monolayer) in presence of water. e–g) Resistance change of $Ru^{(III)}$@MoS_2-NH(Monolayer) and its H_2 response when immersed in water. H_2 response condition: 30 °C, 2000 ppm H_2, Ru 0.5%.*

3.3 In-situ transport of water generated during H_2 detection.

The mechanism underlying the waterproof H_2 sensing capabilities of $Ru^{(III)}$@MoS_2-NH(Monolayer) was illustrated in **Figure 6**. The exceptional waterproof H_2 detection performance was attributed to the integration of hydrophobic monolayer micelles into MoS_2. These micelles not only prevent external water from introducing into the MoS_2 surface, but also effectively mitigated the issue of in-situ water transport

resulting from the H_2-O_2 reaction. This hydrophobic function enhances the sensor's H_2 response, reversibility, and repeatability (**Figure 6a**).

To validate the self-draining mechanism of in-situ produced water, we conducted in-situ FTIR to investigate the behavior of absorbed water over the surface of the $Ru^{(III)}$@MoS_2-NH(Monolayer) sensor during H_2 detection (**Figure 6b**). Preceding H_2 input, we subjected the $Ru^{(III)}$@MoS_2-NH(Monolayer) surface to N_2 cleaning at 80 °C for 30 mins, followed by vacuum treatment for another 30 mins, ensuring no water absorption on the surface. Upon initiating H_2 input, IR signals were recorded over time. Subsequently, trace amounts of water were detected over the surface of $Ru^{(III)}$@MoS_2-NH(Monolayer), evidenced by the appearance and gradual increase of the H_2O peak at 1630 cm^{-1}[25]. This process was attributed to H* from H_2 dissociation over the $Ru^{(III)}$ sites reacting with the absorbed O* on the $Ru^{(III)}$@MoS_2-NH(Monolayer), forming H_2O. This process was also approved by the Raman results (**Figure S10, SI**) with 3232 cm^{-1} after H_2 treatment[26]. However, after a short duration of 5 minutes, the intensity of the H_2O peak begins to decrease, potentially indicating the migration of water from absorbed sites to outside the hydrophobic micelle shell (**Figure 6a**).

The directional transport of in-situ produced water with different micelle layers is further demonstrated by molecular dynamics simulation (**Figure 6c-d**). Water structures at the interface play an important role in the surface properties, which can be illustrated by the density and diffusion profiles[27]. Density profiles of water molecules over the micelle interface are shown in **Figure 6c**. For multilayers, two interfaces at 1 and 3 nm are observed, corresponding to the hydrophilic head of N- at the bottom and

top. In contrast, the monolayer exhibits a peak at 0.9 nm, corresponding to the hydrophilic head of N- at the bottom. These findings align with previous observations, indicating that multilayers distribute hydrophilic heads over the outer layer. Additionally, diffusion coefficients for both monolayer and multilayer systems were calculated **Figure 6d**. Interestingly, the diffusion coefficient of the monolayer is larger than that of the multilayer between 0-4 nm, corresponding to the height of the bilayer micelle. This suggests rapid water transport over the $Ru^{(III)}$@MoS_2-NH(Monolayer), consistent with the in-situ IR results.

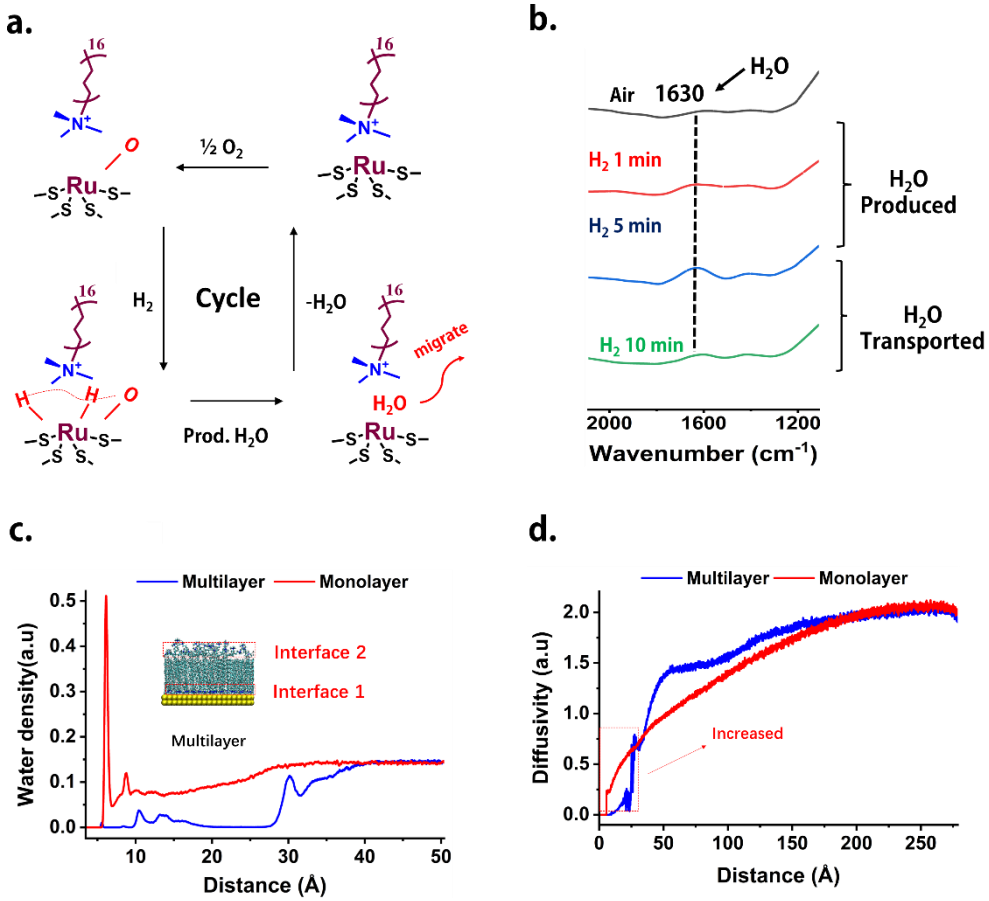

Figure 6. *In-situ produced water directional transport over* $Ru^{(III)}$@MoS_2-*NH(Monolayer) during* H_2 *response. a) Illustration of the self-draining process of* $Ru^{(III)}$@MoS_2-*NH(Monolayer) during* H_2 *response. b) In-situ FTIR of* $Ru^{(III)}$@MoS_2-*NH(Monolayer) during* H_2 *response. Molecular dynamics simulation of c) water*

density and d) diffusion coefficients for $Ru^{(III)}$@MoS_2-NH with monolayer and multilayer micelles. H_2 response condition: 0.5% Ru.

3.4 On-Field inspection H_2 leaks via mobile platform.

Compared to fixed systems, mobile detection systems such as drones and cars provide broad coverage, fast response times, and high-resolution graphical data, quickly identifying and addressing safety hazards associated with H_2 leaks at wide-ranging locations like H_2 fueling stations and chemical plants[28]. Hence, we developed an intelligent inspection system utilizing mobile model platforms such as cars and drones equipped with H_2 sensors, facilitating real-time H_2 leakage monitoring across extensive areas (**Figure 7**).

Based on the exceptional sensing capabilities of the $Ru^{(III)}$@MoS_2-NH(Monolayer) sensor, a prototype wireless H_2 monitoring circuit was developed (**Figure S11a, SI**) that demonstrated lower power consumption and enhanced security. This was achieved by operating at temperatures below 28 °C, contrasting with the 200 °C requirement of commercial H_2 detectors (**Figure S11b-c, SI**). Besides, the sensor was tested in a controlled space under different H_2 concentrations (300-2000 ppm), and real-time feedback was observed on the mobile phone terminal. As depicted in **Figure 7c**, the correlation between signal value and H_2 concentration were made, facilitating a transition for the sensor between signal and concentration readings. Furthermore, the stability of the constructed system demonstrated exceptional performance, enduring up to 6 months without protective membranes against dust and water ingress (**Figure 7d**).

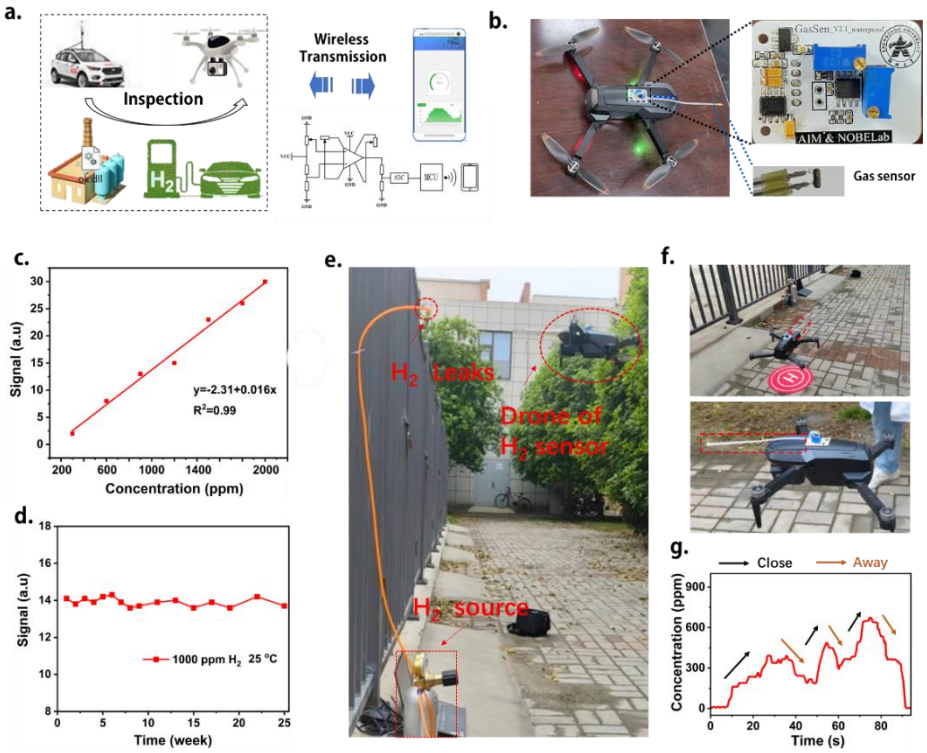

Figure 7. *Wireless H_2 detection of $Ru^{(III)}$@MoS_2-NH(Monolayer) based on mobile platform. a) Schematic diagram of wireless sensing system based on the mobile platform. b) Photos of wireless sensor systems applied to gas leaks searches based on drones and its test circuit. c) Linear fitting curves and d) stability of the wireless H_2 sensor based on the drones. e-f) Photographs for simulation H_2 leak inspection over drone of H_2 sensor and g) its H_2 response curves. H_2 response condition: 30 °C, 0.5% Ru, and 1000 ppm H_2.*

To enhance the practicality of the intelligent inspection system, we introduced this sensor integrated into an artificial car and drone for detecting H_2 leaks (**Figure S12, SI**, and **Figure 7**). For the car, the design included three H_2 leak points, labeled L1, L2, and L3, along the car's S-shaped route. Real-time H_2 responses during the car's movement closely matched the designated path. Expanding the inspection range, drones equipped with this sensor offered high remote inspection capabilities, with H_2 concentration varying along the flight path (both close and away) (**Figure 7e-g**).

Conclusion

In summary, the integration of single-atom $Ru^{(III)}$ self-assembly with hydrophobic monolayer micelles embedded in MoS_2 addresses the longstanding challenge of water fouling in semiconductor-based gas sensors. This innovative approach not only ensures waterproof operation but also significantly enhances the sensor's performance by enabling rapid and accurate H_2 detection. The unique monolayer structure facilitates the self-transport of in-situ generated water, extending the sensor's service life and maintains signal stability of sensor across temperature fluctuations. Additionally, the synergistic effects of $Ru^{(III)}$ and monolayer micelles result in a remarkable reduction in response time. With its capability for wireless detection over extended periods without the need for protective membranes, this work marks a significant advancement in the field, broadening the applicability of semiconductor-based gas sensors in harsh environments.

ASSOCIATED CONTENT

Supporting Information Materials; Preparation of the electrode; Characterization of structure: TEM, XRD, CV, DPV, Raman, In-situ Ramman mapping, Adhesion of AFM; Sensing: Effect of carbon materials and the ratio of Vs-Mo_{S2} to CNT; Kinetic experiment, Single DA molecule force spectrum, DFT calculations.

Author contributions

The manuscript was written through contributions of all authors. All authors have given approval to the final version of the manuscript.

Author information.

Corresponding Author

Acknowledgments.

This work was financially supported by the Young Talent Innovation Team Support Project from Zhengzhou University (No. 32213280),

Competing interests: The authors declare no competing interests.

References

[1] a)I. A. Pereira, *Science* **2013**, 342, 1329; b)A. Magnuson, F. Mamedov, J. Messinger, *Joule* **2020**, 4, 1157; c)M. Losurdo, Y. Gutierrez, A. Suvorova, M. M. Giangregorio, S. Rubanov, A. S. Brown, F. Moreno, *Adv Mater* **2021**, 33, e2100500; d)H. S. Lee, J. Kim, H. Moon, W. Lee, *Adv Mater* **2021**, 33, e2005929.

[2] a)E. Spagnoli, A. Gaiardo, B. Fabbri, M. Valt, S. Krik, M. Ardit, G. Cruciani, M. Della Ciana, L. Vanzetti, G. Vola, S. Gherardi, P. Bellutti, C. Malagu, V. Guidi, *ACS Sens* **2022**, 7, 573; b)I. Darmadi, F. A. A. Nugroho, C. Langhammer, *ACS Sens* **2020**, 5, 3306.

[3] a)A. Sharma, S. B. Eadi, H. Noothalapati, M. Otyepka, H. D. Lee, K. Jayaramulu, *Chem Soc Rev* **2024**, 53, 2530; b)R. A. Potyrailo, C. Surman, N. Nagraj, A. Burns, *Chem Rev* **2011**, 111, 7315; c)A. Tricoli, M. Righettoni, A. Teleki, *Angew Chem Int Ed Engl* **2010**, 49, 7632.

[4] a)X. Li, Z. Gao, B. Li, X. Zhang, Y. Li, J. Sun, *Chemical Engineering Journal* **2021**, 410; b)B. Jiang, T. Zhou, L. Zhang, J. Yang, W. Han, Y. Sun, F. Liu, P. Sun, H. Zhang, G. Lu, *Sensors and Actuators B: Chemical* **2023**, 393, 134257.

[5] F. Qu, S. Zhang, C. Huang, X. Guo, Y. Zhu, T. Thomas, H. Guo, J. P. Attfield, M. Yang, *Angew Chem Int Ed Engl* **2021**, 60, 6561.

[6] a)Y. Wang, Y. Zhou, *Materials (Basel)* **2022**, 15; b)H. Min, O. Kwon, J. Lee, E. Choi, J. Kim, N. Lee, K. Eum, K. H. Lee, D. W. Kim, W. Lee, *Adv Mater* **2024**, 36, e2309041.

[7] J. Xie, L. Zhang, B. Liu, P. Bai, C. Wang, J. Xu, H. Wang, *ACS Appl Mater Interfaces* **2021**, 13, 1956.

[8] a)Z. Song, Z. Huang, J. Liu, Z. Hu, J. Zhang, G. Zhang, F. Yi, S. Jiang, J. Lian, J. Yan, J. Zang, H. Liu, *ACS Sens* **2018**, 3, 1048; b)S. Some, Y. Xu, Y. Kim, Y. Yoon, H. Qin, A. Kulkarni, T. Kim, H. Lee, *Sci Rep* **2013**, 3, 1868.

[9] a)Z. Chen, C. Yu, W. Bai, W. Ye, J. Wang, J. Wei, Y. Wang, J. He, J. Lu, *Sensors and Actuators B: Chemical* **2022**, 372; b)N. K. Arkoti, K. Pal, *ACS Sens* **2024**, 9, 1465.

[10] S. Sayegh, J.-H. Lee, D.-H. Yang, M. Weber, I. Iatsunskyi, E. Coy, A. Razzouk, S. S. Kim, M. Bechelany, *Sensors and Actuators B: Chemical* **2021**, 344.

[11] T. Li, Y. Wu, J. Huang, S. Zhang, *Sensors and Actuators B: Chemical* **2017**, 243, 566.

[12] T. K. N. Pham, J. J. Brown, *ChemistrySelect* **2020**, 5, 7277.

[13] a)Q. Wang, S. Santos, C. A. Urbina-Blanco, W. Y. Hernández, M. Impéror-Clerc, E. I. Vovk, M. Marinova, O. Ersen, W. Baaziz, O. V. Safonova, A. Y. Khodakov, M. Saeys, V. V. Ordomsky, *Applied Catalysis B: Environmental* **2021**, 290, 120036; b)Q. Wang, W.-J. Zhou, S. Heyte, J. Thuriot-Roukos, M. Marinova, A. Addad, S. Rouzière, P. Simon, M. Capron, V. V. Ordomsky, *Chemistry of Materials* **2021**, 33, 8501; c)Q. Wang, C. M. De Brito Mendes, O. V. Safonova, W. Baaziz, C. A. Urbina-Blanco, D. Wu, M. Marinova, O. Ersen, M. Capron, A. Y. Khodakov, M. Saeys, V. V. Ordomsky, *Journal of Catalysis* **2023**, 426, 336.

[14] K. Liu, X. Zhao, G. Ren, T. Yang, Y. Ren, A. F. Lee, Y. Su, X. Pan, J. Zhang, Z. Chen, J. Yang, X. Liu, T. Zhou, W. Xi, J. Luo, C. Zeng, H. Matsumoto, W. Liu, Q. Jiang,

K. Wilson, A. Wang, B. Qiao, W. Li, T. Zhang, *Nat Commun* **2020**, 11, 1263.
[15] D. Wu, Q. Wang, O. V. Safonova, D. V. Peron, W. Zhou, Z. Yan, M. Marinova, A. Y. Khodakov, V. V. Ordomsky, *Angew Chem Int Ed Engl* **2021**, 60, 12513.
[16] Y. Xia, S. Guo, L. Yang, S. He, L. Zhou, M. Wang, J. Gao, M. Hou, J. Wang, S. Komarneni, *Adv Mater* **2023**, 35, e2303523.
[17] R. Wadhwa, A. Kumar, R. Sarkar, P. P. Mohanty, D. Kumar, S. Deswal, P. Kumar, R. Ahuja, S. Chakraborty, M. Kumar, M. Kumar, *ACS Applied Nano Materials* **2023**, 6, 2527.
[18] J. Chen, G. Liu, Y. Z. Zhu, M. Su, P. Yin, X. J. Wu, Q. Lu, C. Tan, M. Zhao, Z. Liu, W. Yang, H. Li, G. H. Nam, L. Zhang, Z. Chen, X. Huang, P. M. Radjenovic, W. Huang, Z. Q. Tian, J. F. Li, H. Zhang, *J Am Chem Soc* **2020**, 142, 7161.
[19] D. Mombrú, M. Romero, R. Faccio, A. W. Mombrú, *Journal of Materials Science: Materials in Electronics* **2018**, 29, 17445.
[20] J. M. Mellott, W. A. Hayes, D. K. Schwartz, *Langmuir* **2004**, 20, 2341.
[21] a)S. J. Singer, G. L. Nicolson, *Science* **1972**, 175, 720; b)L. Shi, K. Li, Y. H. Liu, X. Liu, Q. Zhou, Q. Xu, S. Y. Chen, X. Q. Yu, *Chem Commun (Camb)* **2020**, 56, 3661.
[22] H. G. Girma, K. H. Park, D. Ji, Y. Kim, H. M. Lee, S. Jeon, S. H. Jung, J. Y. Kim, Y. Y. Noh, B. Lim, *Advanced Functional Materials* **2023**, 33.
[23] A. Sanger, A. Kumar, A. Kumar, J. Jaiswal, R. Chandra, *Sensors and Actuators B: Chemical* **2016**, 236, 16.
[24] A. Parastaev, V. Muravev, E. Huertas Osta, A. J. F. van Hoof, T. F. Kimpel, N. Kosinov, E. J. M. Hensen, *Nature Catalysis* **2020**, 3, 526.
[25] V. G. Artemov, E. Uykur, S. Roh, A. V. Pronin, H. Ouerdane, M. Dressel, *Sci Rep* **2020**, 10, 11320.
[26] K. E. Otto, Z. Xue, P. Zielke, M. A. Suhm, *Phys Chem Chem Phys* **2014**, 16, 9849.
[27] a)J. Zhang, J. Tan, R. Pei, S. Ye, Y. Luo, *Journal of the American Chemical Society* **2021**, 143, 13074; b)X.-M. Yu, C.-H. Qi, C.-L. Wang, *Chinese Physics B* **2018**, 27, 060101; c)S. J. Boyd, D. O'Carroll, Y. Krishnan, R. Long, N. J. English, *Crystals* **2022**, 12, 398.
[28] a)D. Terutsuki, T. Uchida, C. Fukui, Y. Sukekawa, Y. Okamoto, R. Kanzaki, *Sensors and Actuators B: Chemical* **2021**, 339, 129770; b)Q. Zhao, W. Zhou, M. Zhang, Y. Wang, Z. Duan, C. Tan, B. Liu, F. Ouyang, Z. Yuan, H. Tai, Y. Jiang, *Advanced Functional Materials* **2022**, 32.